High-efficiency wind-farm-scale wave force estimation for preliminary design of offshore wind installations

W. Wang & A. Kamath
Department of Civil and Environmental Engineering
Norwegian University of Science and Technology, Norway

C. Pákozdi
SINTEF Ocean
Norway

H. Bihs
Department of Civil and Environmental Engineering
Norwegian University of Science and Technology, Norway.

ABSTRACT: Wave load on offshore wind turbines is one of the most important hydrodynamic design factors. Many offshore wind farms are located near the coast, where wave transformation due to bathymetry variations and irregular coastlines lead to a complex hydrodynamic environment. The wave height statistical information does not linearly correlate to the wave loads on wind turbines. Fast calculations to transfer the sea state information to wave loads information are needed for the optimisation of site choice and wind farm configurations. In this article, the authors propose to use the efficient and flexible fully nonlinear potential flow (FNPF) model REEF3D::FNPF to provide large-scale wave environment information. An arbitrary Eulerian-Lagrangian (ALE) method is used to calculate the wave loads on the offshore wind turbines using the non-linear hydrodynamic information from REEF3D::FNPF. The hydrodynamic simulations and force calculations are integrated and performed at run time. The force spectra at all wind turbines in an entire wind farm in an irregular sea can be obtained directly from the simulations. The method provides a holistic overview of the wave forces for an entire wind farm in a computationally- and time-efficient manner. The procedure is a powerful and cost-beneficial tool for the offshore wind industry to optimise the preliminary design of the wind farm installations.

1 INTRODUCTION

Facing the increasing world energy demand, more wind turbines are being constructed in the coastal waters. The support structures of the wind turbines are exposed to complex hydrodynamic loads, especially the wave loads. The evaluation of the wave forces on the wind turbine structures is critical for safe and economically beneficial designs. In order for the realistic evaluation of the wave loads, two steps are required: 1) accurate simulation of the wave field, including wave transformations and non-linear interactions; and 2) accurate calculation of wave forces on structures based on nonlinear hydrodynamics. For a large-scale wind farm, such an evaluation needs computationally efficient models for both the wave field investigation and the wave loads calculation.

Many wave models have been developed for the sea states simulations. The phase-averaged spectra wave models are able to simulate offshore waves efficiently but often not able to resolve the non-linear coastal wave transformations such as diffraction sufficiently (Thomas and Dwarakish 2015). For the representation of the coastal wave transformations, phase-resolving models are needed. The most commonly used phase-resolving models for large-scale coastal waves are based on the shallow water assumption with the depth-averaged approach, such as the Boussinesq-type models (Madsen et al. 1991, Madsen and Sørensen 1992, Nwogu 1993, Madsen and Schäffer 1998, Gobbi et al. 2000, Madsen et al. 2002), non-hydrostatic multi-layer models (Lynett and Liu 2004, Stelling and Duinmeijer 2003, Zijlema and Stelling 2005, Zijlema and Stelling 2008, Zijlema et al. 2011) and quadratic non-hydrostatic pressure models (Jeschke et al. 2017, Wang et al. 2020). However, the accuracy or computational efficiency of these

models deteriorate in deeper water conditions. In contrast, potential flow based models are less restricted by the water depth conditions. Some noticeable models are boundary element models (BEM) (Grilli et al. 1994, Grilli et al. 2001), high-order spectrum (HOS) models (Ducrozet et al. 2012, Bonnefoy et al. 2006a, Bonnefoy et al. 2006b, Raoult et al. 2016, Yates and Benoit 2015) and finite difference method (FDM) based fully nonlinear potential flow models (FNPF) (Li and Fleming 1997, Bingham and Zhang 2007, Engsig-Karup et al. 2009, Bihs et al. 2020). To further increase the stability and flexibility of the potential flow based models near irregular coastal geometry and drastic bathymetry variations, the fully nonlinear potential flow (FNPF) model REEF3D::FNPF introduced various breaking wave algorithms and a novel coastline algorithm and achieved good accuracy and flexibility for both validations and engineering applications (Wang et al. 2022).

For the force calculations, CFD simulations offer the most insights in the fluid-structure interactions but are also very computationally demanding. For the preliminary design of a wind farm, the CFD computational demand is economically expensive and time consuming. Instead, the Morison equation is often used for monopile wind turbine substructures. However, the current practice often uses linear wave theories to approximate the hydrodynamics and thus the resulting estimations are often not sufficient in complex seas. In order to include the high-order wave kinematics such as velocity fields and accelerations near the free surface, an Arbitrary Lagrangian–Eulerian (ALE) framework (Donea et al. 2004) is introduced by Pákozdi et al. (2022) in combined used with the numerical wave model REEF3D::FNPF. Here, the nonlinear wave kinematics are used in the Morison equation for the most realistic representation of the hydrodynamic loads. As REEF3D::FNPF uses the bottom and free surface-following σ-grid in the vertical direction, the mesh moves with the oscillating free surface, the ALE framework can be straightforwardly included. In this way, the force calculations on multiple cylinders are made run-time as the large-scale wave simulations are performed. The hydrodynamic loads on all wind turbines in a wind farm can be estimated simultaneously in an efficient manner.

The hydrodynamic loads are closely associated with the local fluid particle accelerations, and the wave force distribution does not necessarily correspond to the significant wave height distribution, especially with the presence of irregular bathymetry and coastlines. The fast large-scale force calculation is required to give a more realistic understanding of the force distribution on a wind farm. In this article, the FNPF-ALE approach is integrated in the numerical model REEF3D::FNPF and a new procedure for a highly efficient wind-farm-scale wave force estimation method is proposed. A study site at the coast of Norway is used to demonstrate the methodology and the important findings are summarised in the conclusions.

2 NUMERICAL MODEL

2.1 *REEF3D::FNPF*

The potential flow model assumes inviscid and incompressible fluid and irrotational flow. As a result, the fluid particle velocities can be calculated from the velocity potential ϕ. The governing equation to solve for ϕ is the Laplace equation:

$$\frac{\partial^2 \phi}{\partial x^2} + \frac{\partial^2 \phi}{\partial y^2} + \frac{\partial^2 \phi}{\partial z^2} = 0 \tag{1}$$

In order to solve the Laplace equation, boundary conditions are required. As the fluid particles cannot penetrate the solid boundary, the kinematic bottom condition is written as follows:

$$\frac{\partial \phi}{\partial z} + \frac{\partial h}{\partial x}\frac{\partial \phi}{\partial x} + \frac{\partial h}{\partial y}\frac{\partial \phi}{\partial y} = 0. \quad z = -h. \tag{2}$$

At the free surface, two boundary conditions are required: the kinematic free surface boundary condition:

$$\frac{\partial \eta}{\partial t} = -\frac{\partial \eta}{\partial x}\frac{\partial \widetilde{\phi}}{\partial x} - \frac{\partial \eta}{\partial y}\frac{\partial \widetilde{\phi}}{\partial y}$$
$$+ \widetilde{w}\left(1 + \left(\frac{\partial \eta}{\partial x}\right)^2 + \left(\frac{\partial \eta}{\partial y}\right)^2\right), \tag{3}$$

where $\widetilde{\phi}$ is the vertical velocity at the free surface; and the dynamic free surface boundary condition:

$$\frac{\partial \widetilde{\phi}}{\partial t} = -\frac{1}{2}\left(\left(\frac{\partial \widetilde{\phi}}{\partial x}\right)^2 + \left(\frac{\partial \widetilde{\phi}}{\partial y}\right)^2\right)$$
$$+ \frac{1}{2}\widetilde{w}^2\left(1 + \left(\frac{\partial \eta}{\partial x}\right)^2 + \left(\frac{\partial \eta}{\partial y}\right)^2\right) - g\eta, \tag{4}$$

where $\mathbf{x} = (x, y)$ represents the horizontal location and $\widetilde{w}$ is the vertical velocity at the free surface.

The Laplace equation is solved using a finite difference scheme on a σ-grid, which can be transferred from a Cartesian grid as the following:

$$\sigma = \frac{z + h(\mathbf{x})}{\eta(\mathbf{x}, t) + h(\mathbf{x})} \tag{5}$$

The solution is achieved with the conjugated gradient BiCGStab solver (van der Vorst 1992) preconditioned with the geometric multigrid solver PFMG (Ashby and Flagout 1996) provided by hypre.

Through the σ-grid transformation, the particle velocities can be calculated once the velocity potential ϕ is obtained:

$$u\left(\mathbf{x}, z\right) = \frac{\partial\phi\left(\mathbf{x}, z\right)}{\partial x} = \frac{\partial\phi\left(\mathbf{x}, \sigma\right)}{\partial x} + \frac{\partial\sigma}{\partial x}\frac{\partial\phi\left(\mathbf{x}, \sigma\right)}{\partial\sigma}, \quad (6)$$

$$v\left(\mathbf{x}, z\right) = \frac{\partial\phi\left(\mathbf{x}, z\right)}{\partial y} = \frac{\partial\phi\left(\mathbf{x}, \sigma\right)}{\partial y} + \frac{\partial\sigma}{\partial y}\frac{\partial\phi\left(\mathbf{x}, \sigma\right)}{\partial\sigma}, \quad (7)$$

$$w\left(\mathbf{x}, z\right) = \frac{\partial\sigma}{\partial z}\frac{\partial\phi\left(\mathbf{x}, \sigma\right)}{\partial\sigma}. \quad (8)$$

The fifth-order WENO (weighted essentially non-oscillatory) scheme (Jiang and Shu 1996) is used for the spatial derivatives in the free surface boundary conditions and the third-order accurate TVD Runge-Kutta scheme (Shu and Osher 1988) is used for the temporal discretisation. The parallel computation is achieved with the domain decomposition strategy, where MPI (Message Passing Interface) is used for sub-domain communications.

2.2 *Wave generation*

In this work, a relaxation method is used for the wave generation (Mayer et al. 1998):

$$\Gamma(\widetilde{x}) = 1 - \frac{e^{(\widetilde{x}^{3.5})} - 1}{e - 1} \; for \; \widetilde{x} \in [0; 1], \quad (9)$$

where $\widetilde{x}$ is scaled to the dimension of the relaxation zone and the velocity potential ϕ and the surface elevation η are ramped up gradually following the relaxation function:

$$\varphi(\widetilde{x})_{relaxed} = \Gamma(\widetilde{x})\varphi_{analy.} + (1 - \Gamma(\widetilde{x}))\varphi_{compu.}, \quad (10)$$

In the numerical beach, ϕ and η are reduced to still water values following the reversed procedure to minimise the undesired reflection at the outlet boundary.

2.3 *Breaking wave algorithm*

In order to detect breaking waves and dissipate wave energy due to breaking, several breaking criteria are introduced. A steepness-based wave breaking criterion is used for deep water:

$$\frac{\partial\eta}{\partial x_i} \geq \beta. \quad (11)$$

where β is the threshold of wave slope at the wave front.

At shallow water, the depth-induced wave breaking is initialised when the vertical velocity of the free-surface exceeds a fraction of the shallow water celerity (Smit et al. 2013):

$$\frac{\partial\eta}{\partial t} \geq \alpha_s\sqrt{gh}. \quad (12)$$

$\alpha_s = 0.6$ is recommended as it works well with most of the waves (Smit et al. 2013).

After a wave breaking is detected, viscous damping terms are introduced in the free surface boundary conditions as artificial diffusion and thus reduce wave energy. The free surface boundary conditions Eqn. 3 and Eqn. 4 are modified with the added artificial viscosity:

$$\frac{\partial\eta}{\partial t} = -\frac{\partial\eta}{\partial x}\frac{\partial\widetilde{\phi}}{\partial x} - \frac{\partial\eta}{\partial y}\frac{\partial\widetilde{\phi}}{\partial y}$$
$$+ \widetilde{w}\left(1 + \left(\frac{\partial\eta}{\partial x}\right)^2 + \left(\frac{\partial\eta}{\partial y}\right)^2\right) \quad (13)$$
$$+ \nu_b\left(\frac{\partial^2\eta}{\partial x^2} + \frac{\partial^2\eta}{\partial y^2}\right),$$

$$\frac{\partial\widetilde{\phi}}{\partial t} = -\frac{1}{2}\left(\left(\frac{\partial\widetilde{\phi}}{\partial x}\right)^2 + \left(\frac{\partial\widetilde{\phi}}{\partial y}\right)^2\right)$$
$$+ \frac{1}{2}\widetilde{w}^2\left(1 + \left(\frac{\partial\eta}{\partial x}\right)^2 + \left(\frac{\partial\eta}{\partial y}\right)^2\right) - g\eta \quad (14)$$
$$+ \nu_b\left(\frac{\partial^2\phi}{\partial x^2} + \frac{\partial^2\phi}{\partial y^2}\right).$$

where ν_b is the artificial turbulence viscosity. $\nu_b = 1.86$ is used based on the calibrations against CFD models (Baquet et al. 2017).

2.4 *Coastline algorithm*

The detection and treatment of the coastline boundaries are challenging in a potential flow model. In REEF3D::FNPF, it is implemented in a three-step manner. First, the computational cells are identified as wet and dry cells based on a local water depth criterion. When the local total water depth defined in Eqn. (15) is smaller than a user-defined threshold, the cell is considered as a dry cell on land.

$$h^{'} = \eta + h. \quad (15)$$

η is the surface elevation, h is the still water level measured from the bottom.

Thereafter, the wet cells are assigned with a value $+1$ and the dry cells are assigned with a value -1. As all computational cells are signed, the coastline is captured using a level-set function (Osher and Sethian 1988):

$$\phi_{ls}(\vec{x},t) \begin{cases} > 0 \; if \; \vec{x} \in wet \; cell, \\ = 0 \; if \; \vec{x} \in \Gamma, \\ < 0 \; if \; \vec{x} \in dry \; cell. \end{cases} \tag{16}$$

Where Γ indicates the coastline. The Eikonal equation $|\nabla \phi_{ls}| = 1$ holds true at all times.

Finally, relaxation zones are applied following the geometry of the coastline. As a result, the coastline position is fixed, the coastal reflection property can be customised and the numerical stability is improved since the derivative over an infinitesimal water depth is avoided. The coastline algorithm gives realistic representing of complex coastal wave transformation phenomena as presented in Wang et al. (2022)

2.5 *Arbitary Eulerian Lagrangian force calculation*

Instead of costly CFD force simulations or implied Morison calculations, Pákozdi et al. (2022) introduced a fast force calculation approach based on the Arbitary Eulerian Lagrangian (ALE) methods presented by Donea et al. (2004). Here, the material coordinate of a water particle $\vec{X}$ is linked to a fixed Eulerian coordinate $\vec{x}$ by the law of motion:

$$\vec{x} = x(\vec{X},t) \quad at \quad t = t \tag{17}$$

The material velocity $\vec{v}$ is calculated based on the local derivative of x:

$$\vec{v}(\vec{X},t) = \left. \frac{\partial x}{\partial t} \right|_{\vec{x}} \tag{18}$$

where $|_{\vec{x}}$ denotes the material coordinate $\vec{X}$ that is fixed at $\vec{x}$. The motion of the fluid particle is described in a moving frame in the Lagrangian system and a in a time-dependent framework in the Eulerian system. In the ALE coordinate $\vec{\chi}$, the coordinate system moves with a mesh velocity $\vec{\hat{v}}$ equal to the fluid particle velocity $\vec{v}$. This mesh velocity in the Eulerian system is described as the follows:

$$\vec{\hat{v}}(\vec{\chi},t) = \left. \frac{\partial x}{\partial t} \right|_{\vec{\chi}} \tag{19}$$

The fluid particle velocity in the ALE coordinate $\vec{\chi}$ can also be expressed as the following:

$$\vec{w}(\vec{X},t) = \left. \frac{\partial \chi}{\partial t} \right|_{X}. \tag{20}$$

This velocity $\vec{w}$ is the time variation of the ALE coordinate $\vec{\chi}$. The difference between the material and the mesh velocity is then described as a convective velocity $\vec{c}$:

$$\vec{c} = \vec{v} - \vec{\hat{v}} = \frac{\partial \vec{x}}{\partial \vec{\chi}} \cdot \vec{w} \tag{21}$$

where $\vec{c}$ is variation of $\vec{x}$ but $\vec{w}$ is variation of $\vec{\chi}$.

As a result, the fluid particle acceleration $\vec{a} = d\vec{v}/dt$ in an ALE system is expressed as:

$$\vec{a} = \left. \frac{\partial \vec{v}}{\partial t} \right|_{\vec{\chi}} + \vec{c} \cdot \frac{\partial \vec{v}}{\partial \vec{x}} \tag{22}$$

where the convective derivative $\nabla \vec{v} = \frac{\partial \vec{v}}{\partial \vec{x}}$ is usually calculated in the Eulerian system ($\vec{x}$). In the potential flow solver REEF3D::FNPF, the velocity potential is calculated on a σ-grid, which can be treated as an ALE system. Following the description in Eqn. (22), the one-dimensional acceleration in the x-direction can be expressed as:

$$\begin{aligned} a_x = &\left. \frac{\partial u}{\partial t} \right|_{\vec{\sigma}} + u \left(\frac{\partial u}{\partial \xi} + \frac{\partial u}{\partial \sigma} \frac{\partial \sigma}{\partial x} \right) \\ &+ \left(w - \sigma \left. \frac{\partial \eta(x,t)}{\partial t} \right|_{\vec{x}} \right) \frac{\partial u}{\partial \sigma} \frac{\partial \sigma}{\partial z} \end{aligned} \tag{23}$$

where all terms are known in the $\vec{\sigma}$ system and $\vec{\sigma}$ defines the relation ship between the Eulerian and the ALE coordinates:

$$\vec{\sigma} = \begin{bmatrix} \xi \\ \sigma \end{bmatrix} = \begin{bmatrix} x \\ \dfrac{z(t) + h}{h + \eta(x,t)} \end{bmatrix} \tag{24}$$

With the knowledge of the fluid particle acceleration, the Morison force in the x-direction can then be expressed as:

$$\begin{aligned} F_x = &\rho(h + \eta) \\ &\left[\int_0^1 C_M a_x A_{xy} d\sigma + \int_0^1 C_D u|u| \frac{1}{2} B_p d\sigma \right], \end{aligned} \tag{25}$$

where C_M is the inertia coefficient, A_{xy} is the cross-section area, C_D is drag coefficient, B_p is the section breath, h is the still water depth and η is the free surface elevation.

Similarly, the force in the y-direction and the moments can be defined. In this way, forces and moments can be directly calculated from the numerical results in the σ-grid, removing the necessity for further interpolation to a fixed Eulerian frame.

The study case is near Flatøya at the coast of Norway, where a hypothetical wind farm can be constructed, as shown in Fig. 1a. The hypothetical wind farm consists of 24 wind turbines with monopile substructures. The diameter of each monopoly is 6 m, the estimated drag coefficient is 0.9 and the inertia coefficient is 1.5. Here, the red box indicates the study area, where the waves propagate from the north-west direction and diffract around the island of Flatøya. The potential structures are located in the yellow box. By extracting the bathymetry data and align the input wave direction with the input boundary of the numerical wave tank (NWT), the resulting bathymetry in the REEF3D::NFPF NWT is shown in Fig. 1b. The red box to the left hand side is the wave generation zone. The yellow boxes along the other three boundaries are the numerical beaches. The square-shaped computational domain is 4000 m in both x and y-direction. The water depth varies drastically with the deepest point reaching 244 meters. The wave gauges and wind turbine monopiles are shown as yellow dots. Since the ALE approach does not require the physical existence of the structure, the locations of the wave gauges and the monopiles collocate. The wave gauge numbering sequence is indicated by the selected wave gauges.

The input irregular wave has a significant wave height $H_s = 4.0$ m and peak period $T_p = 10.0$ s. The JONSWAP spectrum following the formulation recommended by DNV-GL (DNV 2011) is used as the input design spectrum. Following the grid convergence reccomendations by Wang et al. (2022), the horizontal cell size is 5 m, 10 vertical σ cells are used with a strechign factor of 2.5, resulting in 6.4 million cells in total. The simulation is performed for 3.5 hours where the last 3h time series are used for the following analyses. The free surface elevation at the last time step is shown in Fig. 2. Strong diffraction takes place around Flatøya, creating a cross-sea pattern at the centre of the wind farm. This leads to a complex sea state and makes it challenging to calculate the wave forces based on linear wave theory hydrodynamics.

The significant wave heights at all wave gauges are plotted in Fig. 3a. The maximum total ALE wave forces, defined as $F_{total} = \sqrt{F_x^2 + F_y^2}$, are plotted in Fig. 3b. It's seen that higher waves are observed at the northern and southern boundaries of the wind farm, smaller waves are present in the center of the farm. However, the maximum total wave forces show a different pattern, as seen in Fig. 3b. Here, large wave forces are observed in the center of the domain. This misalignment shows that significant wave height does not linearly corresponds to the wave force. Therefore, the calculation of the wave forces are critical in addition to the investigation of the sea state.
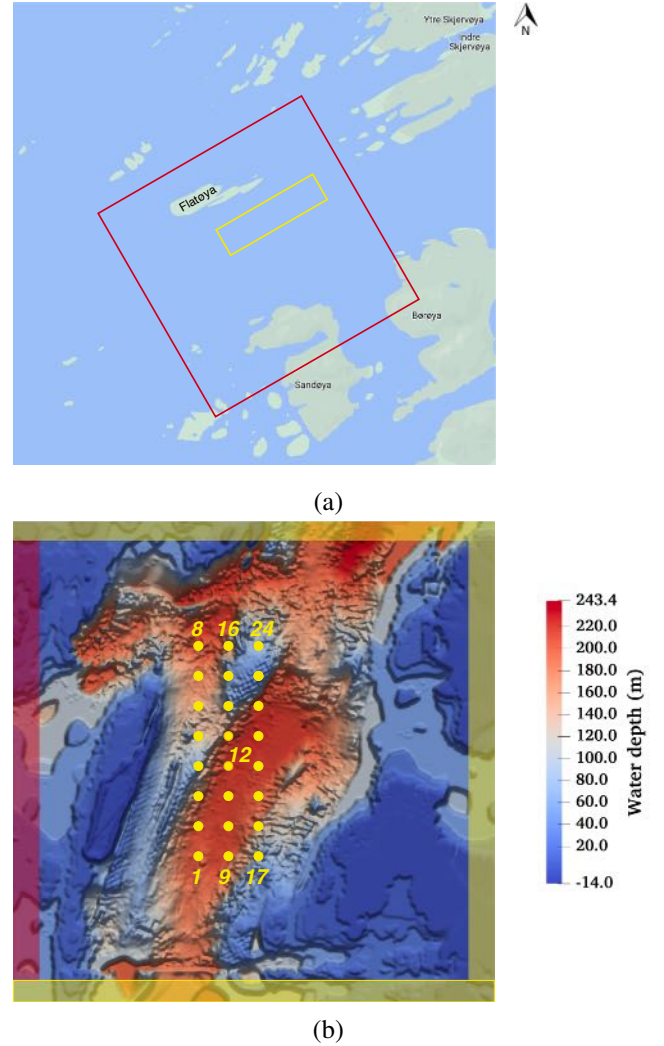

(a)

(b)

Figure 1: (a) the map of the surrounding area near Flatøya, the red box shows the domain of interest, the yellow box shows the hypothetical wind farm location, (b) the numerical wave tank in REEF3D::FNPF with the bathymetry included. The red box shows the wave generation zone, the yellow boxes show the numerical beaches and the yellow dots indicates the locations of the wave gauges as well as the wind turbines.
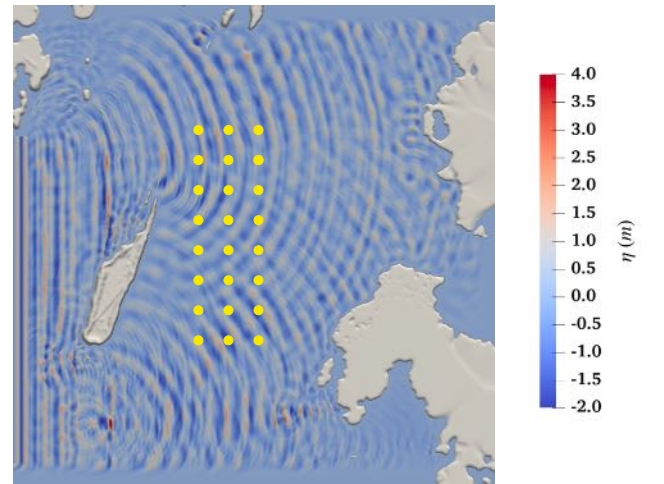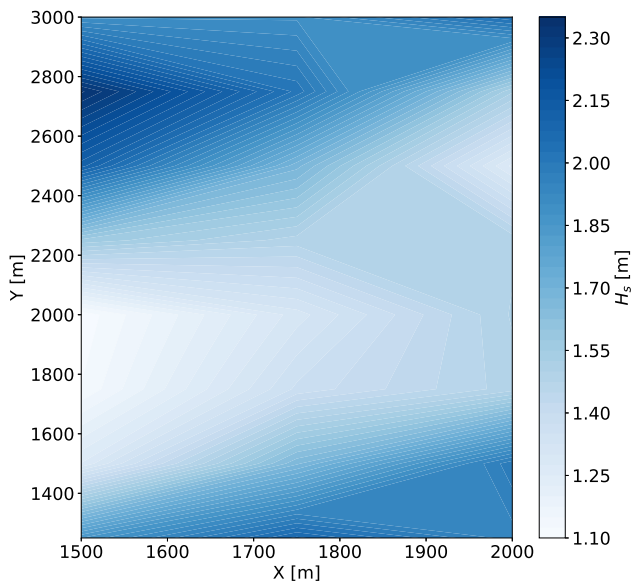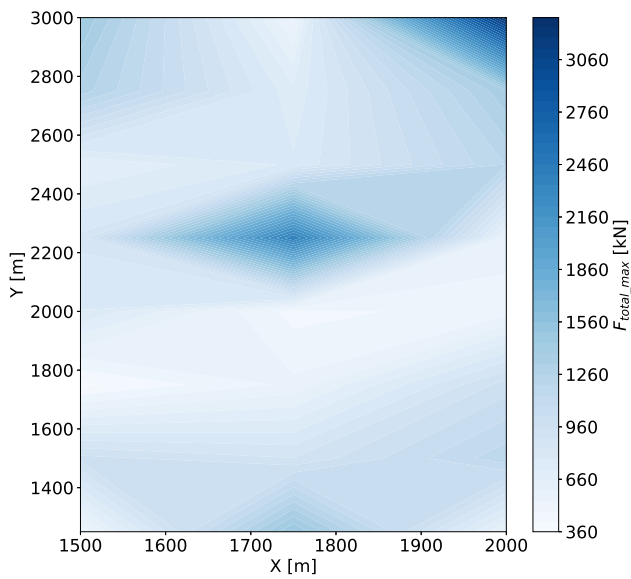

Figure 2: Free surface elevation at the last time step $t = 12800$ s in the simulation of wave propagation near Flatøya.

(a)

(b)

Figure 3: Flatøya.

(a) F_x and F_y time series

(b) wave spectrum

(c) F_x spectrum

(d) F_y spectrum

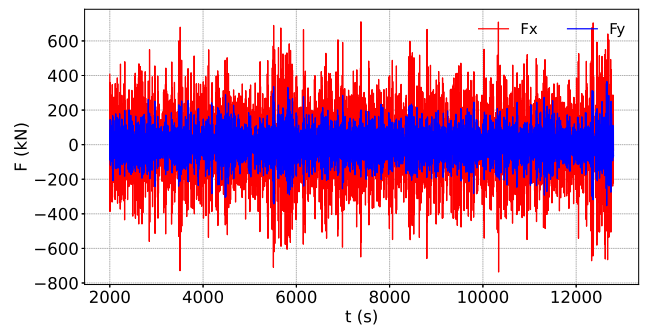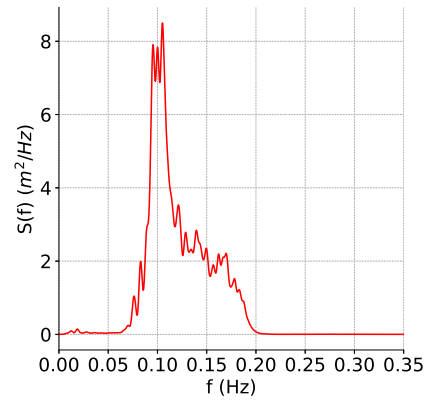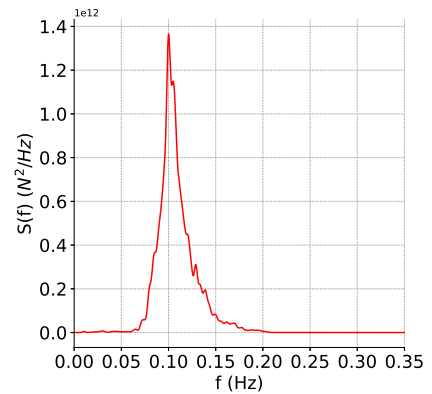Figure 4: The time series of wave forces in x and y directions, the wave spectrum and the wave force spectra in the x and y directions at wave gauge 8.

In order to reveal more details and understand the misalignment between the distribution of H_s and F_{total_max}, monopile number 8 and monopile number 12 are selected for the comparison. In Fig. 4, the time series of wave forces F_x and F_y in x and y directions, the wave spectrum and the wave force spectrum in the x and y directions at wave gauge 8 are plotted. It is seen that the wave force in the x-direction is significantly larger than the y-direction. The F_x spectrum also has a peak frequency the same as the wave peak frequency and the spectrum shape is similar to the wave spectrum. On the contrary, the F_y spectrum has a significant secondary peak in the lower frequency range. It shows that F_x is the dominant force and the force distribution over frequency is different in the x and y directions.
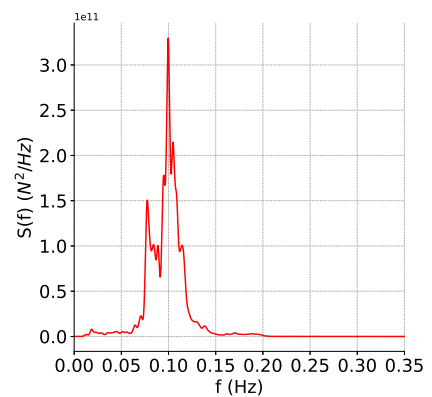
Similarly, the wave field and force information are shown for wave gauge 12 in the centre of the wind farm, as seen in Fig. 5. Here, F_x and F_y have a similar amplitude most of the time according to the time series. As a result, the combined total force tends to
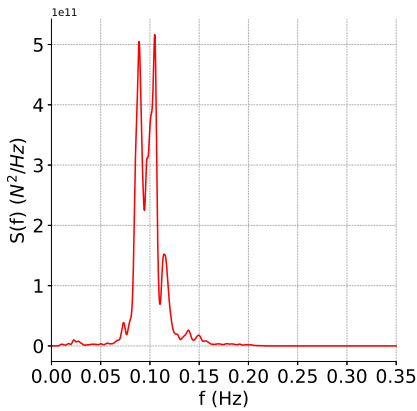
be larger than that at wave gauge 8. Both the wave spectrum and the wave force spectra in the x and y directions have two noticeable peaks, though the two peaks are more predominant for the force spectra.
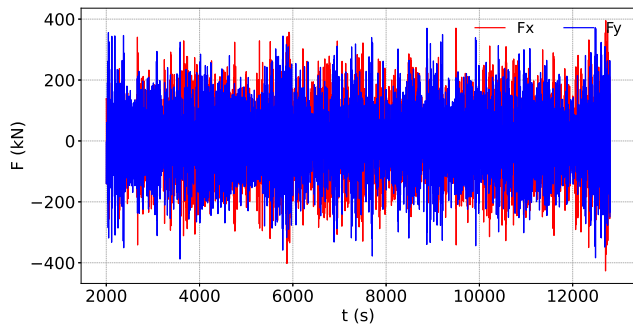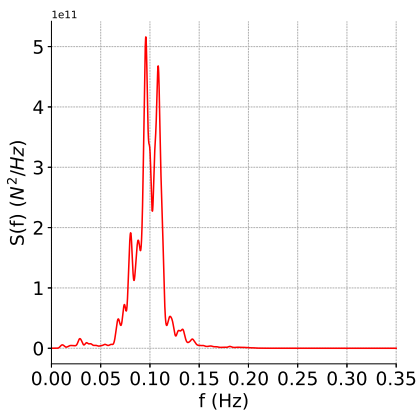

(a) F_x and F_y time series
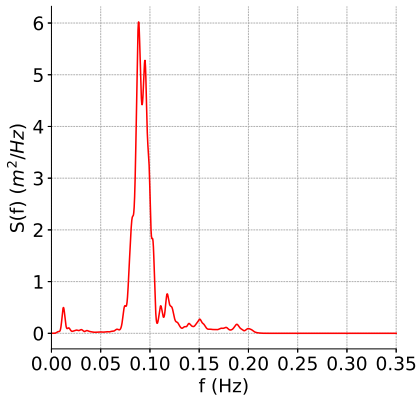
(b) wave spectrum

(c) F_x spectrum

(d) F_y spectrum

Figure 5: The time series of wave forces in x and y directions, the wave spectrum and the wave force spectra in the x and y directions at wave gauge 12.

The different distributions of force components and force spectra are possible reasons that lead to the total force differences in at wave gauge 8 and 12. Since wave forces are closely related to local accelerations, the wave height statistics alone is not a sufficient indicator for the wave forces, especially for such a complex nonlinear wave field with multiple simultaneous wave transformations.

4 CONCLUSIONS

The article uses a fully-nonlinear potential flow (FNPF) model with an Arbitary Eulerian Lagrangian (ALE) force calculation method to evaluate the sea state and predict the forces for a hypothetic wind farm. The FNPF model captures the detailed nonlinear wave transformations near the Flatøya island, especially the predominant diffraction. The force calculations are performed in run-time with the wave simulations. The method does not require the physical presence of the structures, but uses the nonlinear hydrodynamics in the σ-grid of the FNPF model to calculate the wave forces based on the Morison approach. In this way, the wind farm size force evaluation is achieved for the preliminary design of offshore wind installations. The distributions of the significant wave height and the maximum wave forces do not align, stressing the necessity of a fast force estimation in addition to the sea state simulations. The wave force components in the x and y directions and their frequency spectrum both have an influence on the maximum forces. The FNPF-ALE method proves to be an effective way for a large-scale farm-size force calculations with monopoly foundations. Fast force calculations on arbitrary geometry are also planned for the future advancements.

REFERENCES

Ashby, S. F. & R. D. Flagout (1996). A parallel mulitgrid preconditioned conjugate gradient algorithm for groundwater flow simulations. *Nuclear Science and Engineering 124*(1), 145–159.

Baquet, A., J. Kim, & Z. J. Huang (2017, 06). Numerical modeling using CFD and potential wave theory for three-hour nonlinear irregular wave simulations. In *International Conference on Offshore Mechanics and Arctic Engineering*, Volume Volume 1: Offshore Technology, Trondheim, Norway.

Bihs, H., W. Wang, C. Pákozdi, & A. Kamath (2020, 02). REEF3D::FNPF—A flexible fully nonlinear potential flow solver. *Journal of Offshore Mechanics and Arctic Engineering 142*(4), 041902.

Bingham, H. B. & H. Zhang (2007). On the accuracy of finite-difference solutions for nonlinear water waves. *Journal of Engineering Mathematics*, 211–228.

Bonnefoy, F., D. L. Touzé, & P. Ferrant (2006a). A fully-spectral 3d time-domain model for second-order simulation of wave-tank experiments. part a: Formulation, implementation and numerical properties. *Applied Ocean Research 28*(1), 33 – 43.

Bonnefoy, F., D. L. Touzé, & P. Ferrant (2006b). A fully-spectral 3d time-domain model for second-order simulation

of wavetank experiments. part b: Validation, calibration versus experiments and sample applications. *Applied Ocean Research 28*(2), 121 – 132.

DNV (2011, April). Modelling and analysis of marine operations. Standard DNV-RP-H103, Det Norske Veritas, Veritasveien 1, Høvik, Norway.

Donea, J., A. Huerta, J.-P. Ponthot, & A. Rodriguez-Ferran (2004). Arbitrary Lagrangian-Eulerian methods. *Vol. 1*(Chapter 14), pp. 413–437.

Ducrozet, G., F. e. l. Bonnefoy, D. Le Touz é, & P. Ferrant (2012, July). A modified High-Order Spectral method for wavemaker modeling in a numerical wave tank. *European Journal of Mechanics - B/Fluids 34*.

Engsig-Karup, A., H. Bingham, & O. Lindberg (2009). An efficient flexible-order model for 3D nonlinear water waves. *Journal of Computational Physics 228*, 2100–2118.

Gobbi, M. F., J. T. Kirby, & G. Wei (2000). A fully nonlinear boussinesq model for surface waves. part 2. extension to o(kh)4. *Journal of Fluid Mechanics 405*, 181–210.

Grilli, S. T., P. Guyenne, & F. Dias (2001). A fully non-linear model for three-dimensional overturning waves over an arbitrary bottom. *International Journal for Numerical Methods in Fluids 35*(7), 829–867.

Grilli, S. T., R. Subramanya, I. A. Svendsen, & J. Veeramony (1994). Shoaling of solitary waves on plane beaches. *Journal Waterway Port Coastal and Ocean Enigneering 120*(6), 609–628.

Jeschke, A., G. K. Pedersen, S. Vater, & J. Behrens (2017). Depth-averaged non-hydrostatic extension for shallow water equations with quadratic vertical pressure profile: equivalence to boussinesq-type equations. *International Journal for Numerical Methods in Fluids 84*(10), 569–583.

Jiang, G. S. & C. W. Shu (1996). Efficient implementation of weighted ENO schemes. *Journal of Computational Physics 126*, 202–228.

Li, B. & C. A. Fleming (1997). A three dimensional multigrid model for fully nonlinear water waves. *Coastal Engineering 30*(3), 235 – 258.

Lynett, P. & P. L. Liu (2004). A two-layer approach to wave modelling. *Proceedings of the Royal Society of London. Series A: Mathematical, Physical and Engineering Sciences 460*(2049), 2637–2669.

Madsen, P. A., H. B. Bingham, & H. Liu (2002). A new Boussinesq method for fully nonlinear waves from shallow to deep water. *Journal of Fluid Mechanics 462*, 1–30.

Madsen, P. A., R. Murray, & O. R. Sørensen (1991). A new form of the Boussinesq equations with improved linear dispersion characteristics. *Coastal Engineering 15*, 371–388.

Madsen, P. A. & H. A. Schäffer (1998). Higher-order boussinesq-type equations for surface gravity waves: derivation and analysis. *Philosophical Transactions of the Royal Society of London. Series A: Mathematical, Physical and Engineering Sciences 356*(1749), 3123–3181.

Madsen, P. A. & O. R. Sørensen (1992). A new form of the Boussinesq equations with improved linear dispersion characteristics. Part 2. A slowly-varying bathymetry. *Coastal Engineering 18*(3), 183 – 204.

Mayer, S., A. Garapon, & L. S. Sørensen (1998). A fractional step method for unsteady free surface flow with applications to non-linear wave dynamics. *International Journal for Numerical Methods in Fluids 28*, 293–315.

Nwogu, O. (1993). Alternative form of Boussinesq equations for nearshore wave propagation. *Journal of Waterways, Port, Coastal, and Ocean Engineering 119*(6), 618–638.

Osher, S. & J. A. Sethian (1988). Fronts propagating with curvature-dependent speed: Algorithms based on Hamilton-Jacobi formulations. *Journal of Computational Physics 79*, 12–49.

Pákozdi, C., A. Kamath, W. Wang, & H. Bihs (2022). Application of arbitrary lagrangian–eulerian strips with fully nonlinear wave kinematics for force estimation. *Marine Structures 83*, 103190.

Raoult, C., M. Benoit, & M. L. Yates (2016). Validation of a fully nonlinear and dispersive wave model with laboratory non-breaking experiments. *Coastal Engineering 114*, 194 – 207.

Shu, C. W. & S. Osher (1988). Efficient implementation of essentially non-oscillatory shock capturing schemes. *Journal of Computational Physics 77*, 439–471.

Smit, P., M. Zijlema, & G. Stelling (2013). Depth-induced wave breaking in a non-hydrostatic, near-shore wave model. *Coastal Engineering 76*, 1–16.

Stelling, G. S. & S. P. A. Duinmeijer (2003). A staggered conservative scheme for every froude number in rapidly varied shallow water flows. *International Journal for Numerical Methods in Fluids 43*(12), 1329–1354.

Thomas, T. J. & G. Dwarakish (2015). Numerical wave modelling – a review. *Aquatic Procedia 4*, 443 – 448.

van der Vorst, H. (1992). BiCGStab: A fast and smoothly converging variant of Bi-CG for the solution of nonsymmetric linear systems. *SIAM Journal of Scientific Computing 13*, 631–644.

Wang, W., T. Martin, A. Kamath, & H. Bihs (2020). An improved depth-averaged nonhydrostatic shallow water model with quadratic pressure approximation. *International Journal for Numerical Methods in Fluids 92*(8), 803–824.

Wang, W., C. Pákozdi, A. Kamath, S. Fouques, & H. Bihs (2022). A flexible fully nonlinear potential flow model for wave propagation over the complex topography of the norwegian coast. *Applied Ocean Research 122*, 103103.

Yates, M. L. & M. Benoit (2015). Accuracy and efficiency of two numerical methods of solving the potential flow problem for highly nonlinear and dispersive water waves. *International Journal for Numerical Methods in Fluids 77*(10), 616–640.

Zijlema, M. & G. Stelling (2008). Efficient computation of surf zone waves using the nonlinear shallow water equations with non-hydrostatic pressure. *Coastal Engineering 55*(10), 780 – 790.

Zijlema, M., G. Stelling, & P. Smit (2011). SWASH: An operational public domain code for simulating wave fields and rapidly varied flows in coastal waters. *Coastal Engineering 58*(10), 992 – 1012.

Zijlema, M. & G. S. Stelling (2005). Further experiences with computing non-hydrostatic free-surface flows involving water waves. *International Journal for Numerical Methods in Fluids 48*(2), 169–197.